Chemical Science

ROYAL SOCIETY OF CHEMISTRY

EDGE ARTICLE

View Article Online
View Journal | View Issue

Check for updates

Cite this: *Chem. Sci.*, 2025, **16**, 16187

All publication charges for this article have been paid for by the Royal Society of Chemistry

Received 8th February 2025
Accepted 4th August 2025

DOI: 10.1039/d5sc01013f

rsc.li/chemical-science

Design of functionalized tips driven by molecule–plasmon coupling

Huijie He,[a] Xueyang Zhen,[a] Shuang Li,[a] Sibing Chen[a] and Xing Chen *[abc]

The sensitivity of plasmon-enhanced spectroscopy (PES) fundamentally arises from the near-field enhancements within plasmonic nanocavities. To further advance PES, we utilized a molecule with exciton modes that are sensitive to the excitation wavelength to functionalize the metal tip. Our findings reveal that exciton modes play a dominant role in shaping near-field patterns. Specifically, "hot spots" within the exciton mode contribute positively to the near-field enhancements, while "dark spots" provide negative contributions. The functionalized tip exhibits pronounced field gradient effects compared to the bare tip, significantly improving sensitivity and selectivity in near-field spectroscopy. Moreover, both the field enhancement and field gradient effects of the functionalized tip can be effectively tuned by adjusting the excitation energy and tilt angle. These results provide crucial insights into near-field modulation for molecules resonating with plasmonic nanocavities. The development of molecule-functionalized tips offers a promising pathway to advancing PES technology, enabling enhanced sensitivity and selectivity for molecular characterization.

Open Access Article. Published on 04 August 2025. Downloaded on 2/13/2026 3:54:02 AM. This article is licensed under a Creative Commons Attribution-NonCommercial 3.0 Unported Licence.

1 Introduction

The enhanced light–matter interactions in nanocavities driven by plasmonic effects have gained significant attention due to their ability to spatially confine electromagnetic fields at the nanoscale.[1–6] Nanocavity plasmon resonances lead to significant near-field enhancements, which have inspired the development of advanced plasmon-enhanced spectroscopy (PES) techniques,[7,8] including surface-enhanced Raman scattering (SERS),[9–11] tip-enhanced Raman spectroscopy (TERS),[12–18] and surface-enhanced fluorescence (SEF).[19,20] These techniques provide rich chemical information about the composition, structure, and concentration of target substances, which allows for in-depth studies of reaction mechanisms[21–24] and interface interactions,[25–27] providing a deeper understanding of chemical processes at surfaces and interfaces. These techniques have been widely used in reaction control, environmental monitoring,[28–30] sensing applications, and biomolecular interactions. As comprehensively reviewed by Itoh and colleagues,[31] the development of TERS has further enhanced the spatial resolution of Raman spectroscopy, even achieving single-molecule resolution,[32–34] enabling the investigation of molecular behaviors at the nanometer scale with unprecedented precision.[35–37] Furthermore, photo-induced fluorescence spectroscopy has also reached spatial resolution on the sub-nanometer scale, facilitating highly sensitive detection of molecular dynamics and chemical reactions at the molecular level.[38,39]

The sensitivity and resolution of TERS are significantly influenced by the physical and chemical properties of tips. While traditional TERS tips effectively enhance the local electromagnetic field to amplify Raman signal intensity, their sensitivity and applicability are often limited by surface chemistry and molecular selectivity. To address these challenges, functionalization strategies offer a promising solution.[40–42] Through a range of chemical, physical, and biological modifications, likely atomic force microscopy tips, functionalized tips can achieve high molecular selectivity and greater adaptability. For example, techniques like self-assembled monolayers and metal nanoparticle coatings not only strengthen interactions between the tip and target molecules but also enhance the local fields. It is possible to achieve higher resolution and broaden the range of applications in fields such as biological sample analysis, chemical reaction monitoring, and nanomaterials characterization.

To advance TERS, it is essential to understand the factors affecting near-field distributions in systems involving molecules and plasmonic nanocavities. Recent studies have investigated the intricate interactions governing the positioning of molecules within nanocavities.[43,44] TERS signals have been demonstrated to exhibit high sensitivity to the tip's relative position to the target molecule,[45,46] and the surrounding chemical environment.[47] Additionally, variations in the tip–

[a]*Institute of Molecular Plus, School of Chemical Engineering and Technology, Haihe Laboratory of Sustainable Chemical Transformations, Tianjin University, Tianjin 300192, P. R. China. E-mail: xing_chen@tju.edu.cn*

[b]*Haihe Laboratory of Sustainable Chemical Transformations, Tianjin 300192, P. R. China*

[c]*Tianjin Key Laboratory of Low-Dimensional Electronic Materials and Advanced Instrumentation, Tianjin 300192, P. R. China*

© 2025 The Author(s). Published by the Royal Society of Chemistry

Open Access Article. Published on 04 August 2025. Downloaded on 2/13/2026 3:54:02 AM. This article is licensed under a Creative Commons Attribution-NonCommercial 3.0 Unported Licence.

molecule distance can cause significant perturbations in molecular vibrations within the plasmonic nanocavity.[48] Despite these insights, the interactions between resonant single molecules and plasmonic nanocavities, particularly within sub-nanometers, remain inadequately understood. Additionally, most existing studies have focused on configurations where the molecule lies horizontally within the nanocavity, leaving a notable gap in the understanding of molecules adopting vertical orientations or existing in more complex environments. On the other hand, modifying the chemical properties of tips offers a promising alternative. Advanced molecular functionalization techniques have been identified as promising solutions. However, there is limited research focusing on molecule-functionalized tips.[40]

In this work, we elaborately designed a tip functionalized by the pyrrolo[3,4-*c*]pyrrole (pp) molecule. The exciton mode pattern of pp, finely tuned by the excitation wavelength, predominantly governs the near-field distributions in the plasmonic nanocavity. To better understand the interactions between the pp molecule and the nanocavity, we analyzed the contributions from both molecules and nanocavities to the near-field enhancements. The effects of excitation wavelengths and nanocavity separation on the near-field response of the functionalized tip were systematically investigated. Compared to conventional metal tips, the pp-functionalized tip exhibited significant enhancements in field-gradient effects. Furthermore, the impact of tilting the pp molecule on the nanocavity's near-field response is studied, revealing that the tilt can significantly modify the distribution and strength of the field gradient. These enhancements are crucial for improving the selectivity and sensitivity of PES technology, expanding the potential applications of TERS, particularly in fields such as biological sample analysis, chemical reaction monitoring, and nanomaterials characterization, where molecular-level precision is required. By bridging gaps in understanding these interactions, the functionality of TERS tips can be further optimized for more diverse and challenging applications.

2 Methods

In this study, all calculations were performed at 0 K using the Amsterdam Density Functional (ADF) package.[49] For the structure optimization, the Becke three parameter Lee–Yang–Parr (B3LYP) exchange–correlation functional and triple-ζ polarized (TZP) Slater-type basis set with none frozen cores were employed. For the other calculations, the Becke–Perdew (BP86) XC-potential and TZP Slater-type basis set with none frozen cores from the ADF basis set library were used. The polarizability of the molecule–metal system was calculated utilizing the discrete interaction model/quantum mechanical (DIM/QM) method with the local field in ADF.[50] The DIM/QM method integrates QM calculations for molecules with DIM for metal. In this framework, each metal atom is represented as a polarizable sphere, which is polarized by external electric fields. The external electric fields arise from the electron density of the QM part inducing an image-dipole effect and external perturbations inducing a local-field effect. The induced atomic dipoles then perturb the molecular electron density through an embedding operator, leading to a self-consistent solution of the DIM/QM system. This approach overcomes the limitations of traditional macroscopic dielectric models by retaining atomic-level details of the nanoparticle while significantly reducing computational costs through parameterized atomic responses. It has been successfully applied to the simulations of surface-enhanced Raman scattering, plasmonic circular dichroism, and other plasmonic phenomena.[51] In the DIM/QM method, the total polarizability of the system is partitioned into contributions from metal atoms and molecular atoms. The polarizability of metal atoms is further decomposed into image polarizability (α_{image}) and local polarizability (α_{local}). α_{image} arises from image dipoles induced by the molecular charge, reflecting the influence of the molecule on the nanoparticle. α_{local} originates from surface plasmon resonance excited by incident light, representing dynamic polarization effects of collective electron oscillations. The polarizability of molecular atoms is categorized into atomic polarization (local) and interatomic charge flow (nonlocal) contributions by Hirshfeld partitioning.[52] Local polarization refers to the polarization effect generated when the electron cloud of an atom itself distorts relative to the atomic nucleus under the action of an external electric field. Nonlocal polarization is caused by the interatomic charge flow under the action of an external electric field. By independently extracting the atomic polarizabilities of the metal and the molecule, along with their respective components, the contributions of each component to the near-field response in the exciton–plasmon coupling can be analyzed. The damping factor is 0.1 eV during frequency-dependent polarizability calculations. The optical absorption across section at any frequency (ω) can be written as,

$$\sigma_{\text{abs}} = \frac{4\pi\omega n}{c}\text{Im}\{\bar{\alpha}^{\text{NP}}(\omega)\}, \quad (1)$$

where n is the refractive index of the environment (vacuum in this work) and c is the speed of light. In order to correlate the exciton mode pattern to the induced charge density (ρ^{ind}) of the pp molecule, ρ^{ind} is defined by,

$$\rho_z^{\text{ind}} = \frac{\rho_{\alpha_{zz}}\mathbf{E}_0}{r_z}, \quad (2)$$

where ρ_α is the polarizability density. We focused on the α_{zz} component of polarizability density due to the plasmon polarization predominantly occurring along the z direction within the nanocavity. r_z denotes the z-component of the position vector r, where the coordinate origin is defined at the centroid of the pp molecule. $\mathbf{E_0}$ is the incident field, which is typically defined as an external perturbation field that interacts with the system. The near-field at a given position is defined by,

$$E_\alpha = \sum_I^N T_{\alpha\beta}^{(2)}(\mathbf{r})\mu_{I,\beta}^{\text{ind}} + \delta_{\text{ind},\alpha}, \quad (3)$$

where N is the total number of atomic induced dipoles, $\mu_{I,\beta}^{\text{ind}}$ is the atomic induced dipole, which accounts for contributions from all atoms in DIM and QM parts, $\mathbf{r}$ is the vector pointing from the given position to the atomic induced dipole I, and $T_{\alpha\beta}^{(2)}(\mathbf{r})$ is the screened second order interaction tensor. The

© 2025 The Author(s). Published by the Royal Society of Chemistry

Open Access Article. Published on 04 August 2025. Downloaded on 2/13/2026 3:54:02 AM. This article is licensed under a Creative Commons Attribution-NonCommercial 3.0 Unported Licence.

Einstein summation convention is employed for repeated indices. The average near-field magnitude is defined by,

$$|\overline{\mathbf{E}}| = \frac{\sum_{i=1}^{N} |\mathbf{E}_i(r)|}{N}, \quad (4)$$

where N represents the total number of evenly distributed grids within the defined volume. The near-field gradients were calculated by numerical differentiation between the fields at two adjacent grids along each axis. The field gradient magnitude of the near-field along the z-axis is given by,

$$|\nabla E_z| = \sqrt{\left|\begin{matrix} E_z(x+\Delta x) \\ -E_z(x-\Delta x) \end{matrix}\right|^2 \left(\frac{1}{2\Delta x}\right)^2 + \left|\begin{matrix} E_z(y+\Delta y) \\ -E_z(y-\Delta y) \end{matrix}\right|^2 \left(\frac{1}{2\Delta y}\right)^2 + \left|\begin{matrix} E_z(z+\Delta z) \\ -E_z(z-\Delta z) \end{matrix}\right|^2 \left(\frac{1}{2\Delta z}\right)^2} \quad (5)$$

The field gradient effects can be quantified through the ratio of field gradient magnitude to field magnitude (FG ratio). In this work, only the field and field gradient components along the z-axis were considered. Therefore, the FG ratio is written as,

$$R_{\mathrm{FG}} = \frac{|\nabla E_z|}{|E_z|}. \quad (6)$$

The dressed-tensor formalism[53,54] was utilized for the TERS simulations, which involves local fields, field gradients, and derivatives of electric dipole–dipole, dipole–quadrupole, and quadrupole–quadrupole polarizabilities. In this formalism, the molecular transition polarizabilities are dressed as:

$$\alpha^{D,(k)}_{\alpha\beta} = F^{\mathrm{loc},\alpha}_{\gamma}\left[\alpha^{(k)}_{\gamma\delta}F^{\mathrm{loc},\beta}_{\delta} + \frac{1}{3}A^{(k)}_{\gamma,\delta e}F^{\mathrm{loc},\beta}_{\delta e}\right]$$

$$+\frac{1}{3}F^{\mathrm{loc},\alpha}_{\gamma\delta}\left[\mathcal{A}^{(k)}_{\gamma\delta,\varepsilon}F^{\mathrm{loc},\beta}_{\varepsilon} + \frac{1}{3}C^{(k)}_{\gamma\delta,\varepsilon\zeta}F^{\mathrm{loc},\beta}_{\varepsilon\zeta}\right] \quad (7)$$

where $\alpha^{(k)}$, $A^{(k)}$, $\mathcal{A}^{(k)}$, and $C^{(k)}$ are the electric dipole–dipole, dipole–quadrupole, quadrupole–dipole, and quadrupole–quadrupole transition polarizabilities, respectively, for normal mode k, and the Einstein summation convention is assumed for repeated Greek subscripts. The local field of the bare AgNC was simulated using DIM, while those of functionalized tips were modeled using the DIM/QM hybrid approach.[51] In the DIM/QM framework, the pp was treated as the QM part, and the AgNC was represented as the DIM part. The derivatives of electric dipole–dipole, dipole–quadrupole, quadrupole–dipole, and quadrupole–quadrupole polarizabilities with respect to the mass-weighted normal modes were obtained using three-point numerical differentiation.

3 Results and discussion

3.1 Excitons coupled with plasmons

To understand the near-field modulation of the molecule in plasmonic nanocavities, particularly in sub-nanometer-scale cavities where a single molecule is on resonance, we explore the interaction mechanism of the pp molecule coupled with the Ag nanocavity (AgNC). The AgNC is composed of two icosahedral Ag_{309}, each consisting of 309 silver atoms. The selection of pp was driven by its wavelength-dependent near-field properties and its small size, which allows it to orient vertically within the sub-nanocavity. The pp molecule is resonantly excited with the AgNC across the 250–500 nm range (Fig. S1a). Furthermore, the maximal absorption wavelength of bare AgNCs (350 nm) remains unchanged after coupling with pp, regardless of variations in nanocavity separation distances (d) (Fig. S1b).

The exciton mode patterns of the pp molecule are shown in Fig. 1a–d, with their three-dimensional distributions under different excitation wavelengths illustrated in Fig. S2. These patterns illustrate the distinct characteristics of the exciton modes and highlight their sensitivity to the excitation wavelength. The induced charge distributions, depicted in Fig. 1e–l, further elucidate the primary factors driving the variations in exciton mode patterns. Specifically, the real components of induced charge exhibit distinct distributions at different excitation wavelengths, while the imaginary components remain unchanged. These findings suggest that the unique features of exciton mode patterns are predominantly governed by the real component of the induced charge.

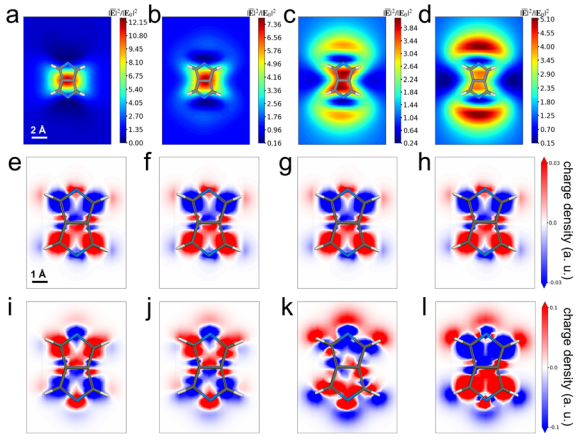

Fig. 1 The exciton modes of free pp at the excitation wavelengths of 338 nm (a), 346 nm (b), 349 nm (c), and 353 nm (d), respectively. The imaginary components of the induced charge density of the free pp at the excitation wavelengths of 338 nm (e), 346 nm (f), 349 nm (g), and 353 nm (h), respectively. The real components of the induced charge density of the free pp at the excitation wavelengths of 338 nm (i), 346 nm (j), 349 nm (k), and 353 nm (l), respectively. Blue represents N atoms, gray represents C atoms, and white represents H atoms.

Open Access Article. Published on 04 August 2025. Downloaded on 2/13/2026 3:54:02 AM.
This article is licensed under a Creative Commons Attribution-NonCommercial 3.0 Unported Licence.

To explore the near-field response of pp in an AgNC (pp@AgNC), we selected various excitation wavelengths to characterize the exciton modes, aligning with those observed in the free molecule. The near-fields distributions in the mid-section of the bare junction under different conditions are presented in Fig. S3. A pronounced gap plasmon forms in the junction with a gap of 9.97 Å. As the gap separation increases, the near-field enhancements diminish, and the gap plasmon gradually transitions into individual dipole plasmons. Although the field enhancements vary across excitation wavelengths, the field distribution patterns remain unchanged. The presence of pp in an AgNC results in a significant increase in the field enhancements (Fig. S4). Moreover, the field distributions of pp@AgNC, with the same gap, exhibit hot spot transfer at different excitation wavelengths. This phenomenon, characterized by molecule-induced hot spot transfer, has been observed experimentally.[55,56] At 342 nm and 350 nm, the fields are predominantly enhanced at the molecular center. In contrast, at 354 nm and 357 nm, the fields are enhanced at both the tip ends and the molecular center, with the intensity varying with the increasing gap distances. These findings indicate the characteristics of the near-field response in pp@AgNC, influenced by both excitation wavelengths and gap separation.

The near-field distribution of pp@AgNC is strongly influenced by the exciton mode of pp. By comparing the near-field distributions of pp@AgNC and the bare AgNC, we characterized the alterations in the near-fields, as shown in Fig. 2. At the excitation wavelengths of 342 nm (Fig. 2a–c) and 350 nm (Fig. 2d–f), substantial field enhancements are observed in the gap center, corresponding to the center of pp, while the fields are diminished in the vicinity of nitrogen atoms in pp. At excitation wavelengths of 354 nm (Fig. 2g–i) and 357 nm (Fig. 2j–l), noticeable field enhancements are observed at the

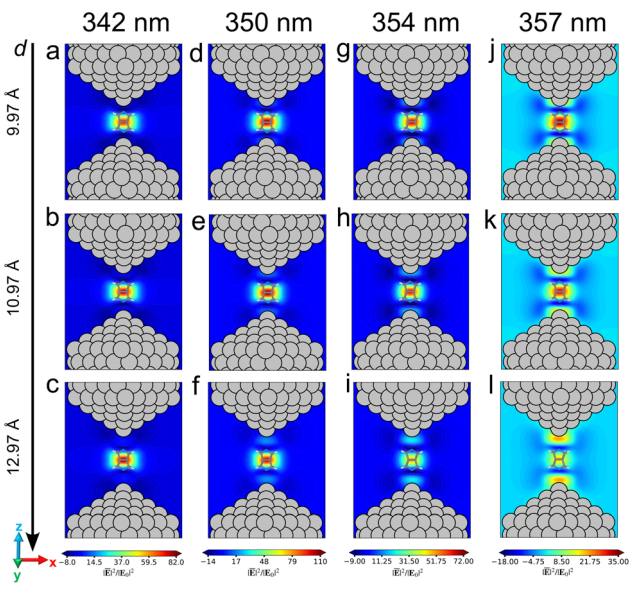

Fig. 2 Field distribution difference between pp@AgNC and the bare AgNC at the excitation wavelengths of 342 nm (a–c), 350 nm (d–f), 354 nm (g–i), and 357 nm (j–l), respectively.

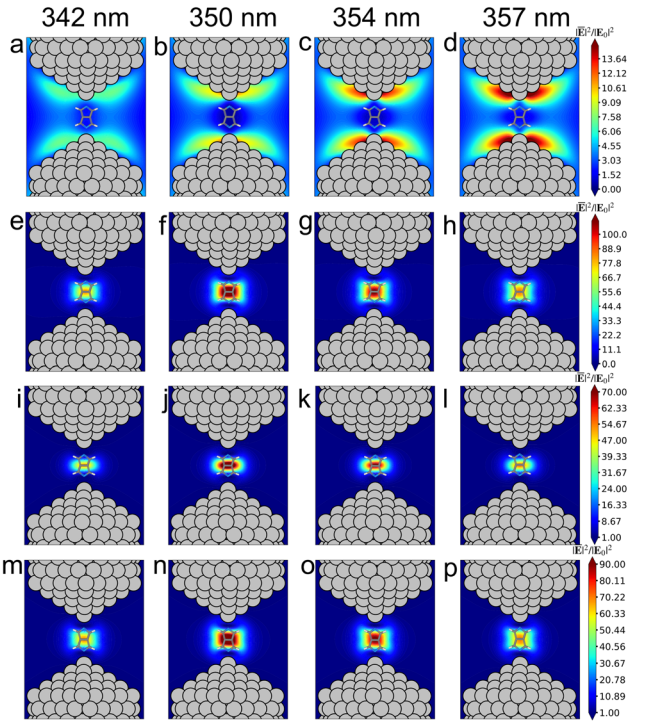

Fig. 3 The partition of near-field distributions of pp@AgNC with the gap size of 9.97 Å into the contributions from the AgNC (a–d) and pp (e–h), contributions of atomic polarization of pp (i–l), and contribution of interatomic charge flow of pp (m–p) under different excitation wavelengths.

AgNC center and both tip ends, while the fields are significantly screened at the ends of pp. The field distribution changes in pp@AgNC are strongly correlated with the exciton modes of pp. In particular, at 342 nm and 350 nm, the exciton modes of pp are characterized by a hot spot in the center of pp (Fig. 1a and b), aligning with near-field pattern variation in pp@AgNC. Similarities are observed at 354 nm (Fig. 1c) and 357 nm (Fig. 1d), indicating that the "hot spots" in the exciton modes positively contribute to the near-fields and "dark spots" negatively affect the near-fields in the AgNC.

Taking pp@AgNC with a gap of 9.97 Å as an example, we analyzed the field enhancements at four excitation wavelengths (Fig. 3). The fields produced by the AgNC under photoexcitation and molecular perturbation, as well as those generated by the molecule under photoexcitation and AgNC coupling, can be derived from the atomic polarizabilities of the AgNC and the molecule, respectively. As illustrated in Fig. 3a–d, the contributions from the plasmon response of the AgNC, characterized by the "hot spots" around the Ag tip, become more prominent at 357 nm. This field distribution aligns with the exciton mode pattern of pp at 357 nm (Fig. 1d). The contributions from the resonant excitation of pp (Fig. 3e–h), characterized by the "hot spots" in the center of the molecule, are particularly pronounced at 350 nm. This enhancement results from the resonant coupling between pp and the AgNC at this wavelength. These findings indicate that the near-fields are most strongly

© 2025 The Author(s). Published by the Royal Society of Chemistry

Open Access Article. Published on 04 August 2025. Downloaded on 2/13/2026 3:54:02 AM. This article is licensed under a Creative Commons Attribution-NonCommercial 3.0 Unported Licence.

enhanced when the plasmon and exciton are both in resonance, and their individual field distributions spatially overlap.

The near-field of the AgNC (9.97 Å) in the presence of pp can be partitioned into two components based on its α_{local} and α_{image}: the local field due to incident light and the image field arising from mutual interactions between the AgNC and pp. As shown in Fig. S5, the local fields are concentrated around the tips, and the image fields are distributed within the junctions. Notably, both the local and image field enhancements increase as the light frequency approaches 357 nm, following a similar trend. Based on the Hirshfeld charge analysis, the molecular contributions to near-fields can be further partitioned into locally polarized near-field dominated by atomic polarization and nonlocal near-field dominated by interatomic charge flows. As the excitation wavelength varies, the near-fields from the local component are mainly localized around the center of pp (Fig. 3i–l), while the near-fields from the charge flow are distributed throughout the molecule (Fig. 3m–p) and are consistently stronger than the local fields. A detailed discussion of individual contributions to near-field distributions within the nanocavity for various gap separations is provided in the SI (Fig. S6 and S7).

3.2 Molecule-functionalized tip

The near-field response of the pp molecule coupled with the AgNC has been discussed. In this section, we examine the characteristics of the molecule-functionalized tip, where pp is attached to the Ag tip. This modification allows for effective tuning of the near-field distribution within the nanocavity, particularly through the excitation wavelength, offering new possibilities for enhancing surface-enhanced spectroscopy techniques. As shown in Fig. 4a and b, the near-field intensity of the molecular-functionalized tip is significantly enhanced at an excitation wavelength of 354 nm, compared to the weaker intensity observed at 342 nm. Furthermore, the near-field distribution of the pp@AgNC tip is highly sensitive to the gap distance between the functionalized tip and the substrate. Notably, the hot spot at the molecular end diminishes as the tip moves further away from the substrate (Fig. S8a–d). These findings indicate the critical role of both excitation wavelength and gap distance in governing exciton–plasmon coupling, which in turn strongly influences the near-field distributions within the plasmonic nanocavity.

To quantify the impact of gap separation on the near-field distribution of the functionalized tip, we analyzed the near-field enhancement and field gradient at a position 2 Å away from the pp-functionalized tip along the *z*-direction, comparing the counterparts under a bare tip. As shown in Fig. 4c, the functionalized tip significantly enhances both the near-field intensity and field gradient. At a gap distance of 10.97 Å, the near-field enhancement of the pp-functionalized tip reaches the maximum. However, as the gap distance increases further, the field enhancement at this position gradually decreases. The FG ratio serves as a key indicator representing the field gradient

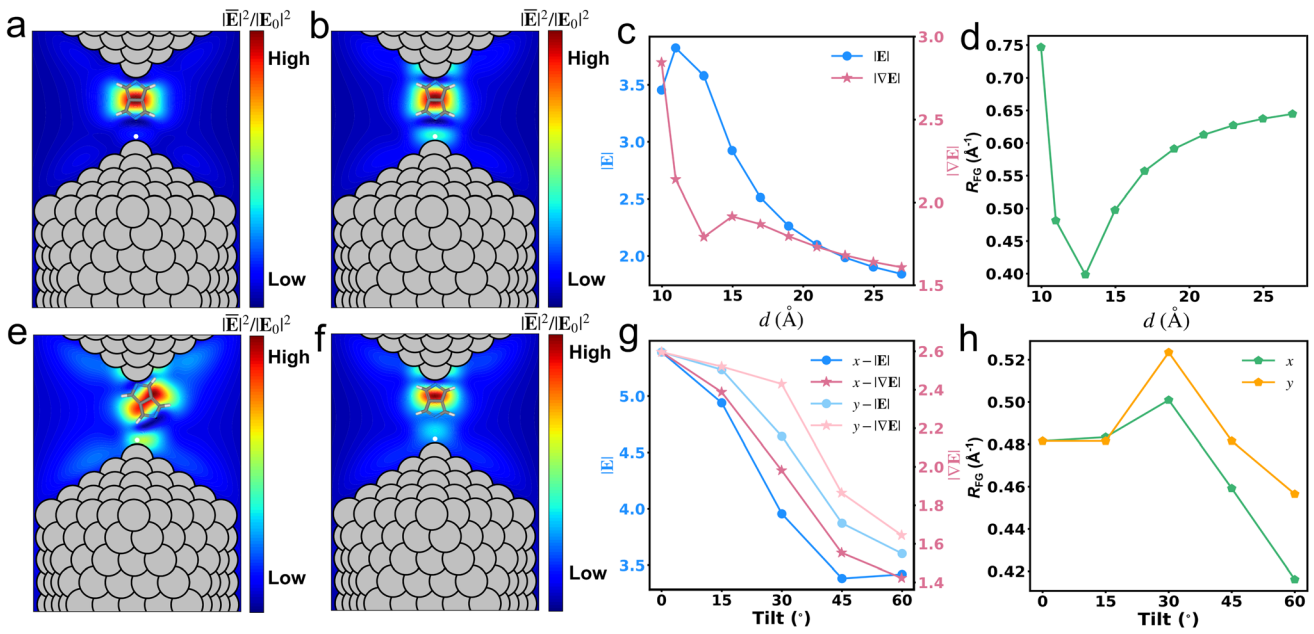

Fig. 4 Near-field distributions of the pp molecule-functionalized tip at a gap size of 10.97 Å under excitation wavelengths of 342 nm (a), 354 nm (b). The white dot marks a characteristic position 2 Å away from the end of the functionalized tip (the N atom on the lower side of the pp molecule). Difference in near-field enhancement and field gradient between the molecule-functionalized tip and the bare tip at a position 2 Å from the functionalized tip end, as a function of gap size at 354 nm (c). The FG ratio of the molecule-functionalized tip at a position 2 Å from the functionalized tip end, as a function of gap size at 354 nm (d). The near-field distributions of the pp-functionalized tip tilted by 30° around the *y*-axis (e) and *x*-axis (f) at a gap size of 10.97 Å, with the white dot position consistent with that in (a). Near-field enhancement and field gradient of the molecule-functionalized tip at the white dot as a function of the tilt angle at 354 nm (g). The FG ratio of the molecule-functionalized tip at the white dot as a function of the tilt angle at 354 nm (h).

Open Access Article. Published on 04 August 2025. Downloaded on 2/13/2026 3:54:02 AM.
This article is licensed under a Creative Commons Attribution-NonCommercial 3.0 Unported Licence.

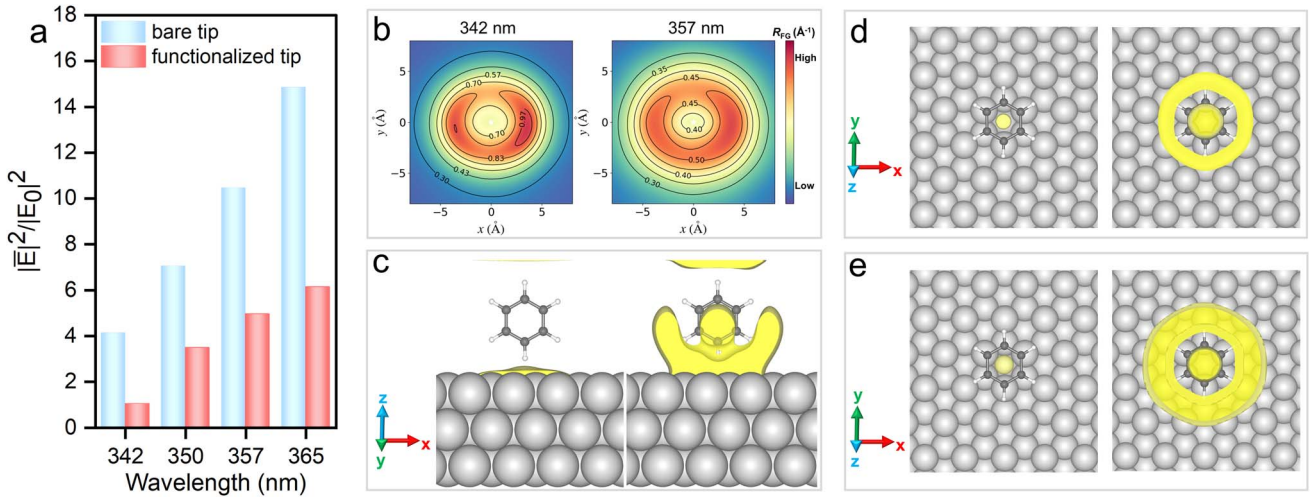

Fig. 5 Comparison of near-field responses of the Ag nanocavity under molecular-functionalized and bare tips with the same tip–molecule distance. Average near-field intensity of functionalized and bare tips in the region of 5 × 5 × 1 Å^3 ($x \times y \times z$) above the Ag substrate (a). Field gradient distributions in the xy-plane under the functionalized tip at excitation wavelengths of 342 nm and 354 nm, with the white asterisk corresponding to the tip position (b). The FG ratio around the vertically orientated benzene molecule in the AgNC at 342 nm, comparing the bare metal tip (left panel) and functionalized tip (right panel) (c). The FG ratio around the horizontally orientated benzene molecule in the AgNC at 365 nm (d) and 342 nm (e), respectively, comparing the bare tip (left panel) and functionalized tip (right panel). The isovalue is set to 1.2 Å^{-1}.

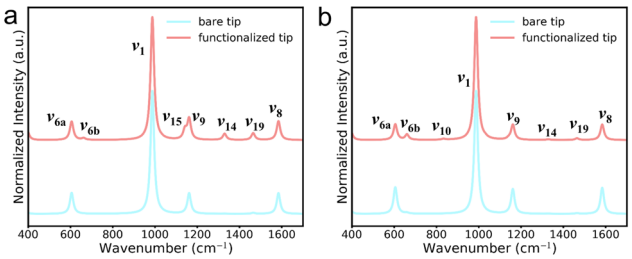

Fig. 6 TERS spectra of a single benzene molecule oriented vertically (a) and horizontally (b) in the AgNC at 342 nm.

effect, which plays a crucial role in PES. The FG ratio at a position 2 Å from the pp-functionalized tip decreases along the z-direction as the gap increases, reaching a minimum at a gap distance of 13 Å, and then it increases again (Fig. 4d). This suggests that tuning the gap of the molecule-functionalized tip effectively modulates both the near-field and the field gradient, thereby optimizing the performance in PES.

Considering that the orientation of the pp molecule on the functionalized tip may vary during experiments, it is important to examine how the tilts influence the near-field response within the plasmonic nanocavity. As shown in Fig. 4, tilting the pp molecule by 30° around the y-axis (Fig. 4e) or x-axis (Fig. 4f) results in significant changes in the near-field distributions. The near-field response at the same reference point, as mentioned earlier, reveals that both the field gradient and near-field enhancement decrease, with their rates of decline differing as the tilt angle increases (Fig. 4g). For tilt angles less than 30°, the reduction in field gradient is less pronounced than the decline in field intensity. For example, a 30° tilt relative to the y-axis results in decreases of 6.4% and 13.9% in the field gradient and near-field enhancement, respectively. In contrast, a 30° tilt relative to the x-axis causes reductions of 23.7% and 26.6%, respectively. For tilt angles in the range of 30° to 60°, the decline in the field gradient exceeds that of the field intensity. Taking 30° as a reference, a 60° tilt relative to the y-axis leads to reductions of 32.4% and 22.3% in the field gradient and near-field enhancement, respectively, while the same tilt relative to the x-axis results in decreases of 28.3% and 13.5%. Consequently, the FG ratio reaches its maximum at a 30° tilt (Fig. 4h). These results demonstrate that the tilt of the molecule-functionalized tip significantly influences the balance between the field gradient and near-field enhancement. This dependency provides an opportunity to finely tune the near-field distribution, potentially enabling precise control over the field gradient effect.

To investigate the near-field response of probe molecules under a molecule-functionalized tip, we assumed a benzene molecule within the nanocavity and analyzed the near-field distribution around it (Fig. S9a and b; note: no benzene molecule was actually introduced in the simulation). In the horizontal direction, we quantified the average near-field intensity within a region (5 × 5 × 1 Å^3) surrounding the benzene molecule and conducted visual analysis on the field gradient across the molecular plane. Since the bare tip can be brought closer to benzene molecules in experiments to enhance the field intensity, we compared the near-field intensities in this region between the two types of tips under the condition of the same tip–molecule distance. The results showed that the average near-field intensity under the functionalized tip is weaker than that under the bare tip (Fig. 5a), and the intensity is more sensitive to the excitation wavelength, as indicated by the rate of change in near-field intensity (Table S1). However, at a fixed Ag nanocavity gap distance, the pp decoration enhanced the near

© 2025 The Author(s). Published by the Royal Society of Chemistry

Open Access Article. Published on 04 August 2025. Downloaded on 2/13/2026 3:54:02 AM. This article is licensed under a Creative Commons Attribution-NonCommercial 3.0 Unported Licence.

fields under excitation wavelengths of 350 nm, 357 nm, and 365 nm (Fig. S10b). Furthermore, the noticeable differences in field gradients under various excitation wavelengths indicate that the field gradient of the functionalized tip can be tuned by adjusting the excitation wavelength (Fig. 5b). This observation highlights the critical role of the pp molecule-functionalized tip in optimizing local field distribution and improving the sensitivity of PES technology.

Subsequently, we placed a benzene molecule with vertical and horizontal orientations relative to the substrate under both the functionalized and bare tips (Fig. S9). A comparison of FG ratios around benzene under the bare tip (Fig. 5c–e, left panel) and functionalized tip (Fig. 5c–e, right panel) reveals the field gradient effect. For a vertically oriented benzene molecule on the substrate, the functionalized tip significantly boosts the field gradient effect, particularly at the center of benzene (Fig. 5c). In contrast, for a horizontally oriented benzene on the substrate, the field gradient effect becomes pronounced around the benzene ring, with its enhancement increasing as the excitation wavelength shifts from 365 to 342 nm (Fig. 5d and e). These findings suggest that vibrational modes with a strong dependence on the field gradient effects will be significantly enhanced in TERS spectra.

To verify the sensitivity of the functionalized tip in molecular spectrum simulation, we carried out simulations of the TERS spectra of benzene molecules using a metal tip and a functionalized tip respectively. The simulation results are shown in Fig. 6. When the benzene molecule is vertically oriented in an AgNC under a functionalized tip (Fig. 6a), it exhibits new TERS signals at 662 cm^{-1}, 1142 cm^{-1}, and 1329 cm^{-1}, compared to the same orientation under a bare metal tip. These signals correspond to the ν_{6b}, ν_{15}, and ν_{14} vibrational modes of benzene, respectively. Meanwhile the intensity of the ν_{19} vibrational mode at 1464 cm^{-1} increases significantly, clearly indicating that the field gradient takes effect.[57] By further examining the benzene molecule horizontally oriented in an AgNC in Fig. 6b, TERS spectra show that under a functionalized tip the signals arising from the ν_{10} (834 cm^{-1}) and ν_{14} (1329 cm^{-1}) vibrational modes are enhanced. Moreover, signals of ν_{6b} and ν_{19} also become prominent. This result further reveals that functionalized tips play a crucial role in probing the field-gradient active signals of the benzene molecule in TERS. It should be noted that the vibration of pp superimposes with that of benzene (Fig. S11a and b). Of course, for a simple molecule like benzene, whose TERS spectrum is dominated by a single band, this superposition is not obvious. However, for generic target molecules, the situation is likely to be more prominent. In addition, the mutual polarization between pp and benzene (Fig. S11c and d) changes the spectral line-shape, but it doesn't significantly affect the main band.

4 Conclusions

In this study, we designed a novel molecule-functionalized tip for enhanced PES applications and investigated the interaction mechanism of the molecule coupled with a plasmon. Our simulations reveal that the field distribution patterns in the nanocavity are predominantly governed by the exciton modes, where "hot spots" contribute positively to the near-field intensity, while "dark spots" inversely affect the fields. We demonstrated the ability to control field distributions and field gradient effects within the nanocavity by manipulating the tip–substrate distance and tuning the excitation wavelength, which are critical for improving selectivity and sensitivity in near-field spectroscopy. Furthermore, the tilt of the functionalized tip significantly influences near-field enhancement and field gradient effects, both of which decrease as the tilt angle increases, with variation in the FG ratio depending on the tilt angle. This research highlights the potential of molecule-functionalized tips as promising tools for designing efficient and sensitive plasmonic devices, paving the way for future advancements in molecular measurement.

Author contributions

X. C. conceived the basic idea, H. H. did the implementation and ran the simulations, X. C., H. H., X. Z., S. L., and S. C. analysed the results, H. H. and X. C. wrote the manuscript.

Conflicts of interest

There are no conflicts to declare.

Data availability

The data supporting this article have been included as part of the SI.

The SI includes the absorption spectra of pp, AgNC, and pp@AgNC, the field distribution patterns of pp, the near-field distributions of AgNC and pp@AgNC, the partition of the near-field distributions of pp@AgNC, the simulation model, the comparison of field intensity change rates, and the comparison of TERS spectra. See DOI: **https://doi.org/10.1039/d5sc01013f**.

Acknowledgements

This work is supported financially by the National Natural Science Foundation of China (Grant 22003047, 22473084). X. C. thanks the Haihe Laboratory of Sustainable Chemical Transformations for financial support and Tianjin University for the startup funding. This work was also partially supported by the Graduate Top-notch Innovation Award Plan in Liberal Arts and Science of Tianjin University (B2-2022-011).

Notes and references

1 X. Chen and L. Jensen, *Nanoscale*, 2018, **10**, 11410–11417.
2 J. T. Hugall, A. Singh and N. F. Van Hulst, *ACS Photonics*, 2018, **5**, 43–53.
3 O. Bitton, S. N. Gupta and G. Haran, *Nanophotonics*, 2019, **8**, 559–575.
4 X. You, W. Peng, J.-X. He, J.-S. Lin, X.-Q. Zong, N. Zhao, J.-L. Yang, M.-D. Li, Y.-J. Zhang, J. Yi, H. Jin, Z.-Q. Tian and J.-F. Li, *Nano Today*, 2022, **45**, 101548.

Open Access Article. Published on 04 August 2025. Downloaded on 2/13/2026 3:54:02 AM. This article is licensed under a Creative Commons Attribution-NonCommercial 3.0 Unported Licence.

5 H. Hu, Y. Xu, Z. Hu, B. Kang, Z. Zhang, J. Sun, Y. Li and H. Xu, *Nanophotonics*, 2022, **11**, 5153–5163.
6 B. Candelas, N. Zabala, P. Koval, A. Babaze, D. Sánchez-Portal and J. Aizpurua, *J. Chem. Phys.*, 2024, **161**, 044707.
7 C. Zhan, X.-J. Chen, J. Yi, J.-F. Li, D.-Y. Wu and Z.-Q. Tian, *Nat. Rev. Chem.*, 2018, **2**, 216–230.
8 R. D. Rodriguez, C. J. Villagómez, A. Khodadadi, S. Kupfer, A. Averkiev, L. Dedelaite, F. Tang, M. Y. Khaywah, V. Kolchuzhin, A. Ramanavicius, P.-M. Adam, S. Gräfe and E. Sheremet, *ACS Photonics*, 2021, **8**, 2243–2255.
9 J. Langer, D. Jimenez De Aberasturi, J. Aizpurua, R. A. Alvarez-Puebla, B. Auguié, J. J. Baumberg, G. C. Bazan, S. E. J. Bell, A. Boisen, A. G. Brolo, J. Choo, D. Cialla-May, V. Deckert, L. Fabris, K. Faulds, F. J. García De Abajo, R. Goodacre, D. Graham, A. J. Haes, C. L. Haynes, C. Huck, T. Itoh, M. Käll, J. Kneipp, N. A. Kotov, H. Kuang, E. C. Le Ru, H. K. Lee, J.-F. Li, X. Y. Ling, S. A. Maier, T. Mayerhöfer, M. Moskovits, K. Murakoshi, J.-M. Nam, S. Nie, Y. Ozaki, I. Pastoriza-Santos, J. Perez-Juste, J. Popp, A. Pucci, S. Reich, B. Ren, G. C. Schatz, T. Shegai, S. Schlücker, L.-L. Tay, K. G. Thomas, Z.-Q. Tian, R. P. Van Duyne, T. Vo-Dinh, Y. Wang, K. A. Willets, C. Xu, H. Xu, Y. Xu, Y. S. Yamamoto, B. Zhao and L. M. Liz-Marzán, *ACS Nano*, 2020, **14**, 28–117.
10 Á. I. López-Lorente, *Anal. Chim. Acta*, 2021, **1168**, 338474.
11 M. Usman, J.-W. Tang, F. Li, J.-X. Lai, Q.-H. Liu, W. Liu and L. Wang, *J. Adv. Res.*, 2023, **51**, 91–107.
12 Z. Liu, S.-Y. Ding, Z.-B. Chen, X. Wang, J.-H. Tian, J. R. Anema, X.-S. Zhou, D.-Y. Wu, B.-W. Mao, X. Xu, B. Ren and Z.-Q. Tian, *Nat. Commun.*, 2011, **2**, 305.
13 S. Bonhommeau and S. Lecomte, *ChemPhysChem*, 2018, **19**, 8–18.
14 R. Meyer, X. Yao and V. Deckert, *TrAC, Trends Anal. Chem.*, 2018, **102**, 250–258.
15 Y. Cao and M. Sun, *Rev. Phys.*, 2022, **8**, 100067.
16 B. Cirera, M. Wolf and T. Kumagai, *ACS Nano*, 2022, **16**, 16443–16451.
17 K. Fiederling, M. Abasifard, M. Richter, V. Deckert, S. Gräfe and S. Kupfer, *Nanoscale*, 2020, **12**, 6346–6359.
18 N. Jiang, E. T. Foley, J. M. Klingsporn, M. D. Sonntag, N. A. Valley, J. A. Dieringer, T. Seideman, G. C. Schatz, M. C. Hersam and R. P. Van Duyne, *Nano Lett.*, 2012, **12**, 5061–5067.
19 J.-F. Li, C.-Y. Li and R. F. Aroca, *Chem. Soc. Rev.*, 2017, **46**, 3962–3979.
20 K. Trofymchuk, K. Kołątaj, V. Glembockyte, F. Zhu, G. P. Acuna, T. Liedl and P. Tinnefeld, *ACS Nano*, 2023, **17**, 1327–1334.
21 C. Zhan, J. Yi, S. Hu, X.-G. Zhang, D.-Y. Wu and Z.-Q. Tian, *Nat. Rev. Methods Primers*, 2023, **3**, 12.
22 R.-P. Wang, B. Yang, Q. Fu, Y. Zhang, R. Zhu, X.-R. Dong, Y. Zhang, B. Wang, J.-L. Yang, Y. Luo, Z.-C. Dong and J. G. Hou, *J. Phys. Chem. Lett.*, 2021, **12**, 1961–1968.
23 C. Zhang, R. B. Jaculbia, Y. Tanaka, E. Kazuma, H. Imada, N. Hayazawa, A. Muranaka, M. Uchiyama and Y. Kim, *J. Am. Chem. Soc.*, 2021, **143**, 9461–9467.
24 S. Tafazoli, M. Yusufoğlu, T. Balkan and S. Kaya, *J. Catal.*, 2023, **423**, 118–128.
25 S.-Y. Ding, J. Yi, J.-F. Li, B. Ren, D.-Y. Wu, R. Panneerselvam and Z.-Q. Tian, *Nat. Rev. Mater.*, 2016, **1**, 16021.
26 L. Li, J. F. Schultz, S. Mahapatra, X. Liu, C. Shaw, X. Zhang, M. C. Hersam and N. Jiang, *J. Am. Chem. Soc.*, 2021, **143**, 15624–15634.
27 Y. Xu, Y. Zhang, C. Li, Z. Ye and S. E. J. Bell, *Acc. Chem. Res.*, 2023, **56**, 2072–2083.
28 H. Wang, X. Huang, G. Wen and Z. Jiang, *Sci. Rep.*, 2019, **9**, 9991.
29 H. Zhang, H. Fu, L. Zhou, P. Zhang, Y. Li and W. Cai, *Nanoscale Horiz.*, 2020, **5**, 739–746.
30 H. Wang, Z. Zhang, C. Chen, A. Liang and Z. Jiang, *J. Hazard. Mater.*, 2021, **403**, 123633.
31 T. Itoh, M. Procházka, Z.-C. Dong, W. Ji, Y. S. Yamamoto, Y. Zhang and Y. Ozaki, *Chem. Rev.*, 2023, **123**, 1552–1634.
32 R. Zhang, Y. Zhang, Z. C. Dong, S. Jiang, C. Zhang, L. G. Chen, L. Zhang, Y. Liao, J. Aizpurua, Y. Luo, J. L. Yang and J. G. Hou, *Nature*, 2013, **498**, 82–86.
33 J. Lee, K. T. Crampton, N. Tallarida and V. A. Apkarian, *Nature*, 2019, **568**, 78–82.
34 Y. Zhang, B. Yang, A. Ghafoor, Y. Zhang, Y.-F. Zhang, R.-P. Wang, J.-L. Yang, Y. Luo, Z.-C. Dong and J. G. Hou, *Natl. Sci. Rev.*, 2019, **6**, 1169–1175.
35 R. Chikkaraddy, B. De Nijs, F. Benz, S. J. Barrow, O. A. Scherman, E. Rosta, A. Demetriadou, P. Fox, O. Hess and J. J. Baumberg, *Nature*, 2016, **535**, 127–130.
36 Y. Zou, G. Song, R. Jiao, G. Duan and L. Yu, *Nanoscale Res. Lett.*, 2019, **14**, 74.
37 Y. Kitajima, H. Sakamoto and K. Ueno, *Nanoscale*, 2021, **13**, 5187–5201.
38 B. Yang, G. Chen, A. Ghafoor, Y. Zhang, Y. Zhang, Y. Zhang, Y. Luo, J. Yang, V. Sandoghdar, J. Aizpurua, Z. Dong and J. G. Hou, *Nat. Photonics*, 2020, **14**, 693–699.
39 S. Gao, R. Zhou, S. Samanta, J. Qu and T. Y. Ohulchanskyy, *Anal. Chim. Acta*, 2023, **1254**, 341086.
40 N. Friedrich, A. Rosławska, X. Arrieta, K. Kaiser, M. Romeo, E. Le Moal, F. Scheurer, J. Aizpurua, A. G. Borisov, T. Neuman and G. Schull, *Nat. Commun.*, 2024, **15**, 9733.
41 J. Lee, N. Tallarida, X. Chen, L. Jensen and V. Apkarian, *Sci. Adv.*, 2018, **4**, eaat5472.
42 N. Tallarida, J. Lee and V. A. Apkarian, *ACS Nano*, 2017, **11**, 11393–11401.
43 F. Zhang, J. Yi, W. Peng, P. M. Radjenovic, H. Zhang, Z. Tian and J. Li, *Angew. Chem.*, 2019, **131**, 12261–12265.
44 X. Wang, S.-C. Huang, S. Hu, S. Yan and B. Ren, *Nat. Rev. Phys.*, 2020, **2**, 253–271.
45 S. Duan, G. Tian, Y. Ji, J. Shao, Z. Dong and Y. Luo, *J. Am. Chem. Soc.*, 2015, **137**, 9515–9518.
46 X. Chen, P. Liu, Z. Hu and L. Jensen, *Nat. Commun.*, 2019, **10**, 2567.
47 B. Yang, G. Chen, A. Ghafoor, Y. Zhang, X. Zhang, H. Li, X. Dong, R. Wang, Y. Zhang, Y. Zhang and Z. Dong, *Angew. Chem., Int. Ed.*, 2023, **62**, e202218799.

© 2025 The Author(s). Published by the Royal Society of Chemistry

Open Access Article. Published on 04 August 2025. Downloaded on 2/13/2026 3:54:02 AM.
This article is licensed under a Creative Commons Attribution-NonCommercial 3.0 Unported Licence.

48 R. B. Jaculbia, H. Imada, K. Miwa, T. Iwasa, M. Takenaka, B. Yang, E. Kazuma, N. Hayazawa, T. Taketsugu and Y. Kim, *Nat. Nanotechnol.*, 2020, **15**, 105–110.
49 AMS 2023.1, SCM, *Theoretical Chemistry*, Vrije Universiteit, Amsterdam, The Netherlands, **http://www.scm.com**.
50 J. L. Payton, S. M. Morton, J. E. Moore and L. Jensen, *J. Chem. Phys.*, 2012, **136**, 214103.
51 Z. Hu and L. Jensen, *J. Chem. Theory Comput.*, 2018, **14**, 5896–5903.
52 F. L. Hirshfeld, *Theor. Chim. Acta*, 1977, **44**, 129–138.
53 D. V. Chulhai, X. Chen and L. Jensen, *J. Phys. Chem. C*, 2016, **120**, 20833–20842.
54 J. Lee, N. Tallarida, X. Chen, P. Liu, L. Jensen and V. A. Apkarian, *ACS Nano*, 2017, **11**, 11466–11474.
55 M. Wan, J. Wu, J. Liu, Z. Chen, P. Gu, P. Zhan, Z. Wang and S. I. Bozhevolnyi, *Nanotechnology*, 2021, **32**, 035205.
56 J.-X. Zhang, Q.-S. Meng, G. Chen, Y. Zhang, Y. Zhang and Z.-C. Dong, *ACS Photonics*, 2023, **10**, 3682–3690.
57 D. V. Chulhai and L. Jensen, *J. Phys. Chem. C*, 2013, **117**, 19622–19631.

© 2025 The Author(s). Published by the Royal Society of Chemistry